Journal of Materials Chemistry A

Accepted Manuscript

ROYAL SOCIETY OF CHEMISTRY

www.rsc.org/materialsA

Journal Name

ARTICLE

Structural evolution of NASICON-type $Li_{1+x}Al_xGe_{2-x}(PO_4)_3$ using *in situ* synchrotron X-ray powder diffraction

Received 00th January 20xx,
Accepted 00th January 20xx

DOI: 10.1039/x0xx00000x

www.rsc.org/

Dorsasadat Safanama,[a] Neeraj Sharma,[b] Rayavarapu Prasada Rao,[a] Helen E. A. Brand,[c] and Stefan Adams[a]

Fast Li-ion conducting $Li_{1+x}Al_xGe_{2-x}(PO_4)_3$ or LAGP ceramics are the most commonly used anode-protecting membranes in a new generation of Li-air batteries. The electrochemical properties of this solid membrane (electrolyte) are highly dependent on the purity of the phase and the actual amount of Al incorporated into the structure which often deviates from the synthetic inputs for different annealing conditions. Hence, optimizing the annealing temperature range is of great importance to achieve desirable phases and therefore optimized properties. Here *in situ* synchrotron X-ray diffraction is undertaken during the synthesis of LAGP. Starting with ball-milled and calcined LAGP glass powders we observe the structural evolution during the glass to ceramic transition. Sequential Rietveld refinements show that the dominant Al-poor LGP phase transforms into an Al-incorporated LAGP structure at temperatures higher than 800 °C. The *c* lattice parameter is found to be highly dependent on the temperature and also the amount of Al incorporated into the structure. The relationship between the *c* lattice parameter and Al concentration in LAGP is evaluated and the correlation can be used to allow estimation of Al doping. Thus this work allows the lattice parameter to "fingerprint" the dopant concentration.

Introduction

New generations of Lithium-based batteries[1, 2] and among them aqueous and hybrid Li-air batteries (LABs) aim to offer not only energy densities which are significantly higher than those of conventional rechargeable battery systems, but to combine the outstanding energy density with an attractive power performance. The power performance and cycle life of an aqueous Li-air battery is essentially determined by the fast lithium-ion conducting solid that is employed to protect the lithium anode from reacting chemically with the catholyte solution.[3, 4] A wide range of fast-ion conducting oxide[5-7] and sulfide[8-10] solid electrolytes and their applications[11, 12] have been explored over the past decades.[13] Moreover, the suitability of these solids as anode-protecting membranes has been the subject of detailed discussion.[4, 14, 15] A crucial drawback is that most of these solids are prone to undergo H^+ for Li^+ exchange in contact with aqueous catholyte solutions.[16-18] Among various classes of solid electrolytes, NASICON-type fast Li-ion conducting ceramics[19-22] have found the most wide spread use for application as anode-protecting membranes,[23-25] and incidentally are also explored as solid electrolytes in conventional all-solid-state lithium secondary-batteries.[26, 27]

NASICON-type $LiM_2(PO_4)_3$ (M = Ge, Ti, Sn, Zr and Hf)[28, 29] has an open three-dimensional framework of alternating corner sharing PO_4 tetrahedra and MO_6 octahedra (Fig. 1(a)). This framework leaves two distinct types of sites for the lithium: The 6*b* Li(1) site is located at the inversion centre (on the $\bar{3}$ axis) between two MO_6 units and is surrounded by 6 oxygen atoms in trigonal antiprismatic coordination, and six of the 36*f* Li(2) site pairs (surrounding a 18*e* site) with an irregular 6+6-fold oxygen coordination are grouped around each Li(1) site. For the rhombohedral (space group *R*-3*c*) undoped $LiGe_2PO_4$, Li(1) sites are reported to be fully occupied leaving Li(2) sites empty.[30] For the isostructural Al-doped $Li_{1+x}Al_xGe_{2-x}(PO_4)_3$ (LAGP), the charge imbalance introduced by a partial substitution of Al^{3+} for Ge^{4+} is compensated by additional Li^+ ions which occupy the Li(2) site. For the case of the isostructural $Li_{1+x}Al_xTi_{2-x}(PO_4)_3$ as well as for analogous Na-containing NASICON phases it has been found that the additional monovalent cations also lead to a cation redistribution from the Li(1) to the Li(2) site.[21] This can be understood as a consequence of the reduced difference of Li (or Na) site energies when both sites are partially occupied, *viz* it is energetically favourable for Li (or Na) to be dispersed in a more even concentration over the two sites rather than one site being fully occupied and the other partially occupied.[21, 31] Bond valence site energy (BVSE) calculations presented in Fig. 1(b) show that Li(1) and Li(2) are the only low energy Li sites in the LAGP structure (as well as in the large group of isostructural NASICON-type solid electrolytes). Furthermore, the Li^+ migration pathway of lowest activation energy is a

[a] National University of Singapore, Department of Materials Science and Engineering, Singapore 17579, Singapore. Email: mseasn@nus.edu.sg
[b] University of New South Wales, School of Chemistry, Sydney, NSW 2052, Australia.
[c] Australian Synchrotron, Clayton, Victoria 3168, Australia.

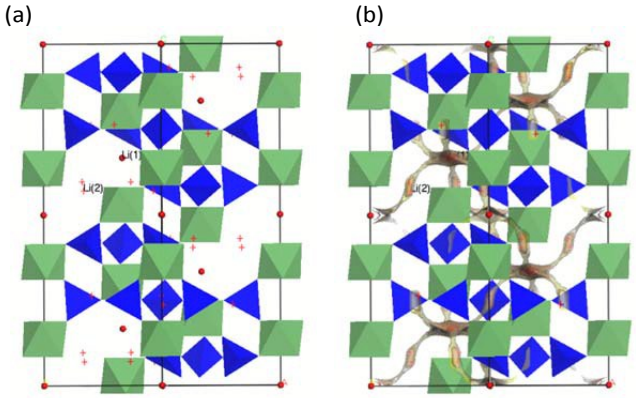

Fig. 1 (a) Schematic representation of $LiGe_2(PO_4)_3$ structure (GeO_6, green; PO_4, blue, Li(1): red spheres, Li(2): red crosses) (b) Bond-valence site energy pathway model for Li^+ ion migration in crystalline LAGP. Yellow isosurfaces represent structure regions that Li+ ions can reach with an activation barrier of 0.35 eV.

three dimensional pathway network involving both site types: each Li(1) site is connected via the 6 surrounding Li(2) site pairs to 6 adjacent Li(1) sites.

In 1991, Alami et al.[30] studied the temperature dependence of the undoped $LiGe_2(PO_4)_3$ structure in the temperature range of 300-1000 K using neutron powder diffraction and presented a model for the anisotropic thermal expansion and its relation with the Li site distribution. One of the most established methods to synthesize NASICON-type solid electrolytes is by a solid-state reaction: A glass of the desired stoichiometry is produced by melt quenching and subsequent heat treatment is carried out to ensure crystallization.[32, 33] Such a controlled crystallization of the solid electrolyte from a homogeneous glass yields a ceramic of more uniform and dense microstructure with desirable mechanical properties. Schröder et al.[34] looked into the crystallization of $Li_{1+x}Al_xGe_{2-x}(PO_4)_3$ glasses for different dopant contents x by solid state NMR. Accordingly, the incorporation of Al into the structure causes an expansion of the MO_6 coordination polyhedron and, for nominal compositions with x > 0.5, $AlPO_4$ is formed as an impurity phase. Recently, Abri et al.[35] proposed based on room temperature X-ray diffraction (XRD), NMR and impedance spectroscopy that the increase of Li^+-ion conductivity with Al content in Al-doped samples is caused by the increase in the lithium content resulting in a reduced energetic preference for Li(1) site occupancy. The authors also highlighted that the amount of Al that is actually incorporated into the LGP structure and hence contributes to the enhanced ionic conductivity will often deviate substantially from the nominal Al content yielding a wide scatter of literature performance data. Therefore, there appears to be an intimate relationship between conductivity (performance), lithium site occupation, Al incorporation and synthesized composition, microstructure and quite possibly impurities. De-convoluting these facets and identifying the relationships between them will allow us to make better materials.

To the best of our knowledge there is no *in situ* structural study on the crystallization of the Al-doped LAGP glasses. Therefore, we have studied the formation of LAGP ceramics from a glassy precursor of the same overall chemical composition by *in situ* synchrotron XRD. These studies will help to rationalize the synthesis process, enhance its reproducibility and energy efficiency and yield guidelines on how to improve the phase purity and reduce dopant inhomogeneities, as well as provide details on the deviations between nominal and actual Al dopant concentrations.

Experimental

NASICON-type $Li_{1+x}Al_xGe_{2-x}(PO_4)_3$ (LAGP) glass was prepared using melt quenching method as described elsewhere.[36] In brief, stoichiometric amounts of Li_2CO_3 (Alfa Aesar, Ward Hill, MA), Al_2O_3 (Sigma Aldrich, Milwaukee, WI), GeO_2 (Alfa Aesar, Ward Hill, MA) and $NH_4H_2PO_4$ (Merck) were mixed and ball-milled (Fritsch Pulverisette 7) using zirconia bowls and balls, pre-heated to 700 °C, molten at 1450 °C and quenched using stainless steel plates (as the heat sink). The resulting glass was ground again for further characterization.

In situ synchrotron X-ray powder diffraction (s-XRD) was carried out to investigate the formation of crystalline LAGP from the ground glass sample. The Powder Diffraction beamline (10-BM-1) at the Australian Synchrotron was used for these experiments.[37] This beamline is equipped with a MYTHEN microstrip detector and a Si(111) monochromator. The wavelength λ of the X-ray beam was calculated to be λ = 0.72721(4) Å using the NIST 660b LaB_6 standard reference material. The powdered glassy precursor was packed in 0.3 mm quartz capillaries and heated using a hot air blower at a rate of 1 °C per minute to 425 °C, then at a rate of 2 °C per minute to per minute to 750 °C and kept at this temperature for 2 hours. Subsequently the temperature was raised to 950 °C with the same heating rate 2 °C/min. Cooling from 950 °C was undertaken at 5 °C per minute. During this annealing cycle, data were continuously collected for two minutes per diffractogram accounting for 2 - 10 °C depending on the rates used. LAMP was employed for visualization of the data.[38] Sequential Rietveld refinements of *in situ* s-XRD data were undertaken using the GSAS suite of programs[39] with the EXPGUI interface.[40] The number of refinable variables was reduced by the use of constraints: All atomic positional parameters and atomic displacement parameters (ADPs) for Ge and Al atoms in the LAGP phase and ADPs for O atoms were set to be equal. The background was modelled by refining 10 parameters using the shifted Chebyshev function (function 1 in GSAS). For the first dataset at the highest temperature and hence full crystallization, lattice parameters, atomic positional, ADPs and occupancies were refined. Note that ADPs and occupancies were not refined simultaneously, ADPs were fixed while occupancies were refined and vice versa. During the separate sequential refinements of heating and cooling runs, ADPs were kept fixed. The total crystalline phase fraction of the glass ceramics was estimated as the sum of the unit cell mass weighted absolute scale factors for all

crystalline phases in a specific pattern, divided by the corresponding value for the plateau reached after full crystallization around T = 820 °C. Absolute phase fractions for each individual crystalline phase are then calculated by multiplying the mass fraction of this phase (out of all crystalline phases) extracted from the Rietveld refinement with the crystalline phase fraction.

Results and discussions

Fig. 2(a) shows a two-dimensional (2D) intensity colour map of *in situ* s-XRD data vs. time along with the temperature variation for the formation of LAGP ceramic from the glassy precursor sample of nominal composition of $Li_{1.5}Al_{0.5}Ge_{1.5}(PO_4)_3$. The glass sample was heated from room temperature to 750 °C and kept at this temperature for 2 hours followed by subsequent heating to 950 °C. As can be seen in the map, the sample starts to crystallize at about 570 °C.

Selected s-XRD patterns during crystallization are presented in Fig. 2(b). Details of the 17.3° < 2θ < 17.7° (d ≈ 2.4 $Å^{-1}$) range in the XRD patterns are shown in Fig. 3(a) and Fig. 3(b) for the initial phase of the crystallisation between 578 °C

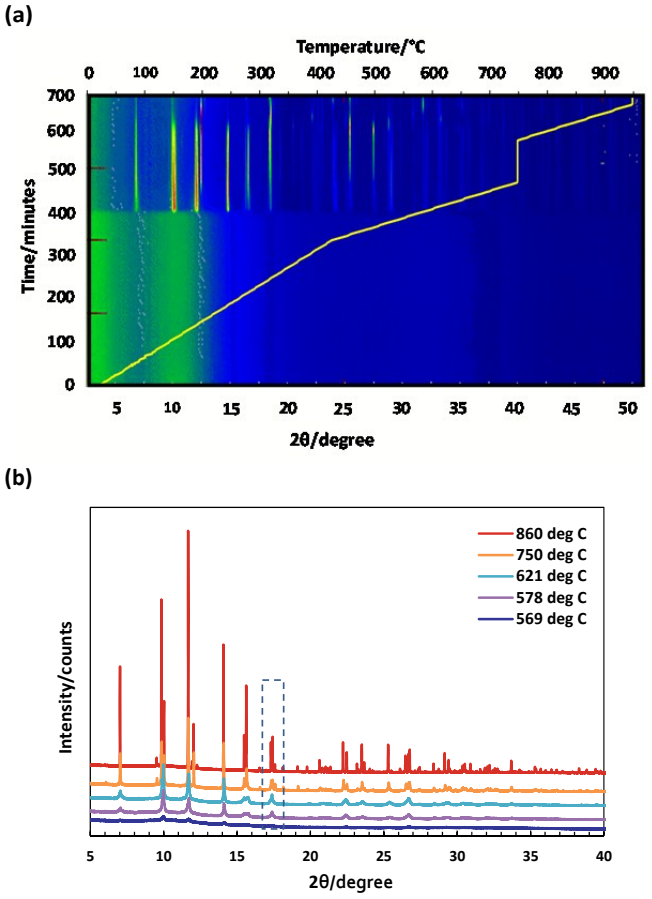

Fig. 2 (a) Two dimensional intensity colour map for s-XRD data vs. time. The solid yellow line indicates the temperature variation during the heat treatment cycle. (b) Changes in the s-XRD pattern during prolonged crystallization (the box highlights the (214) peak (d ≈ 2.4 $Å^{-1}$) addressed in detail in Fig. 3).

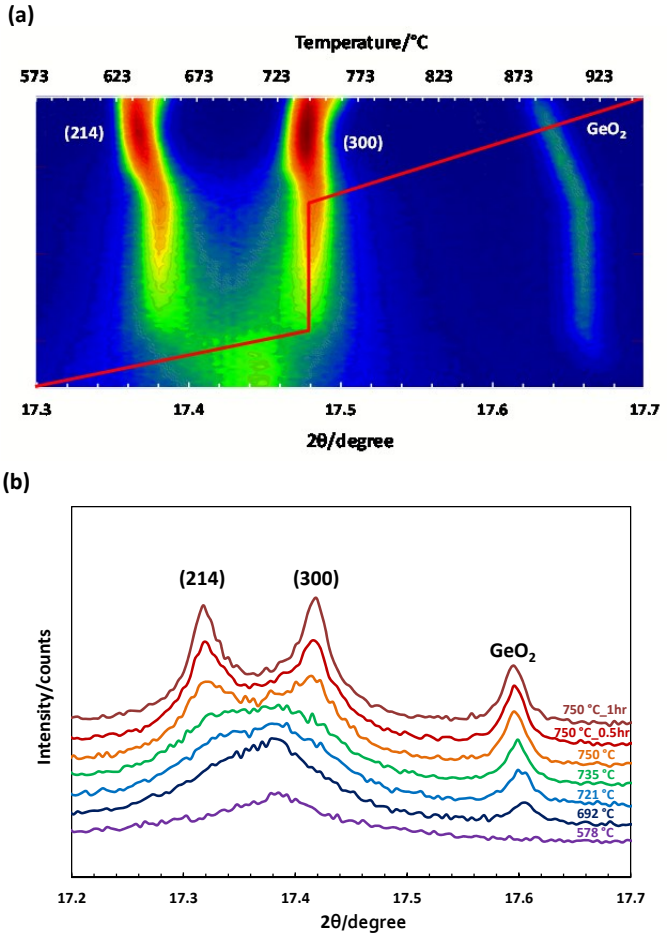

Fig. 3 Phase evolution for the (214) peak during the heating cycle in (a) 2D map for the collected data and (b) selected s-XRD patterns

and 750 °C as a 2D map and individual patterns. Clearly the nature of the main crystalline phases changes with increasing temperature: In the initially formed NASICON phase the (214) and (300) peaks overlap almost completely, while the quantity (refined phase fraction) of this phase drastically shrinks on continued heating to around 730 °C. At this point, a new NASICON phase with a more pronounced splitting of the (214) and (300) peaks, i.e. with a distinct *c:a* lattice parameter ratio, becomes the majority phase. This process is accompanied by the formation of a new peak at 2θ = 17.6° which is later identified as GeO_2 suggesting that the phase formed around 730 °C probably is Ge-deficient.

To further investigate this phase evolution, a detailed Rietveld analysis is performed. The Rietveld refinement of structural models for the s-XRD pattern of the sample at T = 578 °C shows that at this early stage of crystallization the sample is composed mainly of two phases of Al-poor $LiGe_2(PO_4)_3$ ("LGP", a_{hex} = 8.3205(4) and c_{hex}=20.571(2)) as the majority crystalline phase and Al-rich $Li_{1+x}Al_xGe_{2-x}(PO_4)_3$ ("LAGP", a_{hex}=8.2951(4) and c_{hex}=20.835(2)) as the minority crystalline phase, both crystallizing in the rhombohedral space group $R\bar{3}c$. The low values of the residual wR_p of 6.5 % and of

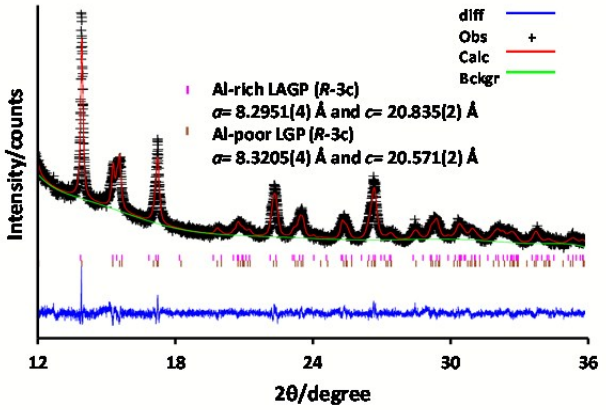

Fig. 4 Rietveld refinement of powder s-XRD pattern for the glass-ceramic sample at 578 ^{0}C during the heating cycle (+++) observed, (—) calculated and difference. Vertical bars correspond to the calculated Bragg reflections from *R*-3c model for LAGP (top) and LGP (bottom)

χ^2 = 1.94 confirm the good agreement between our structural models and the experimental data (Fig. 4).

Fig. 5(a) shows the changes in the absolute phase fractions (wt%) of the crystalline phases along with the amorphous phase fraction and impurity phases for the temperature range of 568°C to 950 °C in the heating run from the sequential Rietveld refinements. On increasing the temperature, Al incorporation into the LAGP phase gradually progresses and the Al-rich LAGP phase becomes the dominant phase at the expense of the decreasing fractions of both the Al-poor LGP phase and the amorphous content. From the mass fractions of the different crystalline products the average composition of the amorphous content varies during the course of the crystallization process from $Li_{1.5}Al_{0.5}Ge_{1.5}(PO_4)_3$ to about $Li_2AlP_3O_{10}$.

A closer look into the evolution shows that around the temperature of 670 °C (when LAGP has just become the majority phase) the rate of phase formation decreases. In addition, the LGP phase fraction continues to decrease but this is now accompanied by the formation of the secondary phase GeO_2 (space group of $P3_12_1$) up to 750 °C (see Fig. 5(b)). The heat treatment program maintained the sample at 750 °C for two hours and during this dwell time the incorporation of Al from the amorphous phase into the LAGP phase was nearly completed. This yielded a more homogeneous phase of LAGP and a pronounced reduction of the LGP phase fraction. As the observed change in LAGP/LGP phase ratio is accompanied by a pronounced decrease in strain broadening (from 0.18% to below the resolution limit, see Fig. 6), it may be tentatively assumed that both phases were present in the same particle.

Interestingly, during the 750 °C dwell the residual amorphous phase crystallizes yielding $Li_4P_2O_7$ (space group $P\bar{1}$) as an impurity phase. Upon further heating beyond 800 °C, the phase fraction of this $Li_4P_2O_7$ impurity phase decreases (possibly through a reaction with the GeO_2 impurity); and there is no trace of this phase left in the sample at 816 °C. It can therefore be assumed that the existence of this impurity phase in the final sample can be avoided if sufficient time is provided during annealing above 816 °C (Fig. 5(b)).

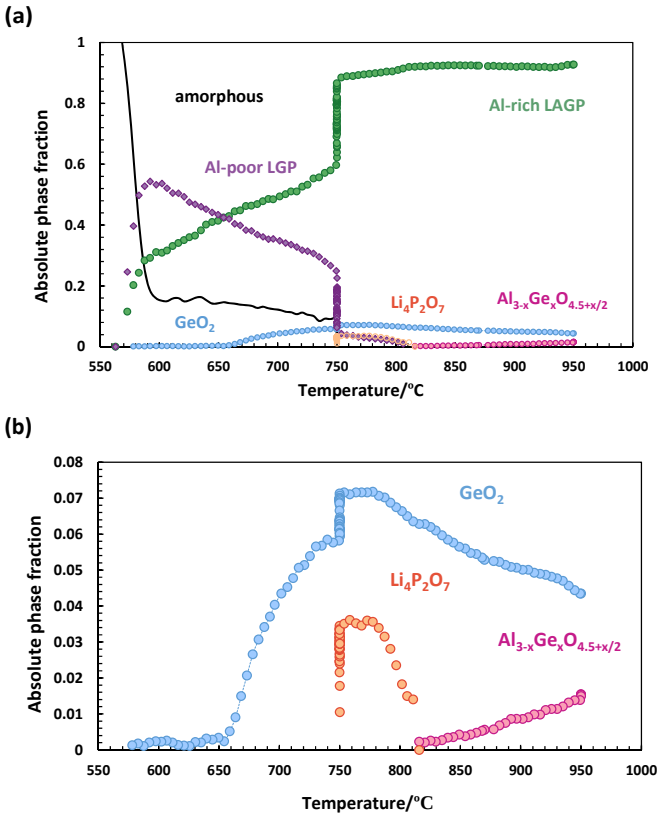

Fig. 5 Temperature dependence of absolute phase fractions (a) Al-rich LAGP and Al-poor LGP phases along with impurity phases and (b) impurity phases of GeO_2, $Li_4P_2O_7$ and $Al_{3-x}Ge_xO_{4.5+x/2}$ during heating.

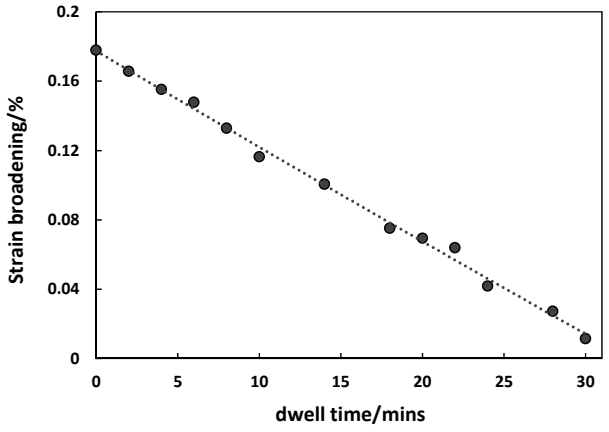

Fig. 6 Changes in the strain broadening of LAGP phase with dwell time.

For temperatures above 800 °C, the Al-poor LGP phase disappears completely and NASICON-type LAGP is the dominant crystalline phase. Even though crystallization of LAGP sets in at 568 °C, our results demonstrate that for "complete" incorporation of Al into the structure the sample should be annealed at temperatures above 800 °C. As shown in Fig. 5(b), the phase fraction of GeO_2 also starts to decrease, around 800 °C, which in turn raises the phase fraction of the main LAGP phase. Increasing the temperature further is however detrimental, as above 820 °C a new Al-rich impurity phase, germanium mullite $Al_{3-x}Ge_xO_{4.5+x/2}$ (space group

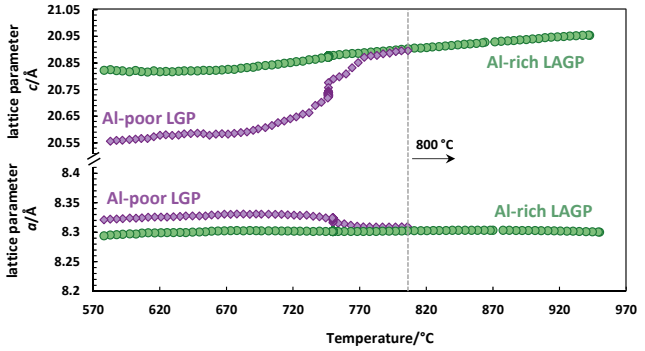

Fig. 7 Temperature dependence of lattice parameters 'c' and 'a' for the Al-poor and Al-rich NASICON phases.

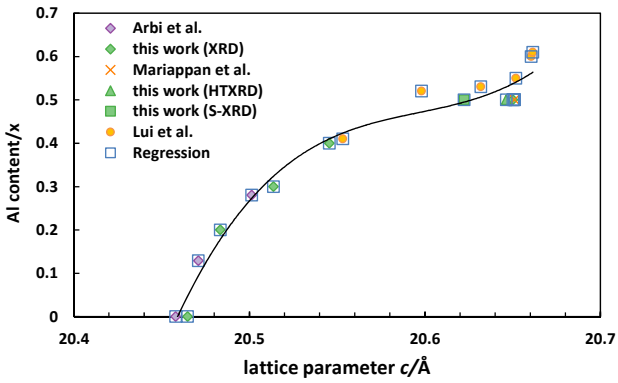

Fig. 8 Room temperature lattice parameter *c* for LAGP samples with varying Al content (*x* in $Li_{1+x}Al_xGe_{2-x}(PO_4)_3$) (Data from literature is extracted from [35], [41] and [42]).

*I*4/*mcm*), is formed. As discussed below, the formation of $Al_{3-x}Ge_xO_{4.5+x/2}$ concurrently leads to a depletion of Al from LAGP.

The temperature dependences of the lattice parameters *a* and *c* for the two main phases LGP and LAGP are shown in Fig. 7. For both phases, heating the sample results in a preferential expansion of the lattice along the *c* axis. Alami et al. [30] attribute this elongation of the *c*-axis to rotations of the nearly rigid PO_4 groups in NASICON-type LGP around the Li(1) site. Only a minor increase occurs in the lattice parameter *a* for temperatures exceeding 900 K. The same trend is observed in our data for Al-poor LGP. For LAGP the lattice parameter *c* increases by heating the sample while the lattice parameter *a* remains nearly constant. The pronounced non-linearity of the thermal expansion might indicate that slight changes of the Al content and distribution also play a role for the change in this lattice parameter up to about 750 °C. For temperatures above 770 °C, i.e. after the dwell period, a more homogeneous Al-distribution in the sample is not only implied by the drastic reduction of the phase fraction of LGP, but also by the fact that the lattice parameters of the two phases "LAGP" and "LGP" become nearly identical before the "LGP" vanishes completely. In this temperature range, where we may assume that the composition of the phase remains constant, the linear thermal expansion coefficient along the *c*-direction assumes a value of $\alpha_c = 19\times10^{-6}\ K^{-1}$ while the expansion coefficient for the perpendicular direction is significantly smaller $\alpha_a \approx 3\times10^{-6}\ K^{-1}$.

Apart from temperature, the lattice parameter *c* – as mentioned above – also strongly depends on the amount of Al incorporated into the LAGP phase. Fig. 8 shows the variation in *c* parameter for different Al contents for the *ex situ* samples (x between 0 and 0.6) along with the data extracted from literature. Accordingly, Al doping results in an expansion along *c* axis in the structure. The actual amount of Al doping usually deviates from the synthetic input values. Arbi et al.[35] found that the actual Al-content extracted from MAS-NMR spectra in their samples differed significantly from the synthetic input values (x = 0.280 for the synthetic input value of x = 0.5) and the deviation is larger for higher synthetic input values. Regression analysis presented here can be used to derive the actual Al content x in a LAGP sample to an accuracy of ±0.03 from the value of the lattice parameter *c* using equation (1):

$$x = 137.951773\ c^3 - 8523.82837\ c^2 + 175558.931\ c - 1205290.72 \quad (1)$$

The '*c*' lattice parameter values of our samples (based on synthetic input compositions) show good agreement with those for actual compositions reported by Arbi et al. based on NMR analyses, therefore we may assume that deviations between the nominal and actual Al content are within the accuracy limits of the above calibration curve.

Keeping the sample at 950 °C for 30 minutes results in a continued depletion of Al from LAGP into the mullite impurity phase and this leads to a phase transition, as evidenced by the formation of shoulders of the LAGP phase peaks (Fig. 9). We suspect that the Al loss by keeping the sample at 950 °C predominantly changes the composition in the surface region of the particles. Thereby the sample again contains two phases of Al-rich and Al-poor NASICON-phases, where now the Al-poor phase can be identified with the outer shell of the particle, while the particle bulk still consists of Al-rich LAGP. Rietveld refined s-XRD pattern at the end of the 950 °C dwell is presented in Fig. 10.

Data is also collected for the sample during cooling at 5 °C from 950 °C to room temperature. Fig. 11 shows the s-XRD patterns for the 2θ range of 20.5 to 21.8 degrees for 4 selected temperatures. We attempted to elucidate any subtle structural changes on cooling, especially a transition to the monoclinic LT-NASICON phase, as reported for $LiHf_2(PO_4)_3$.[43] However, we

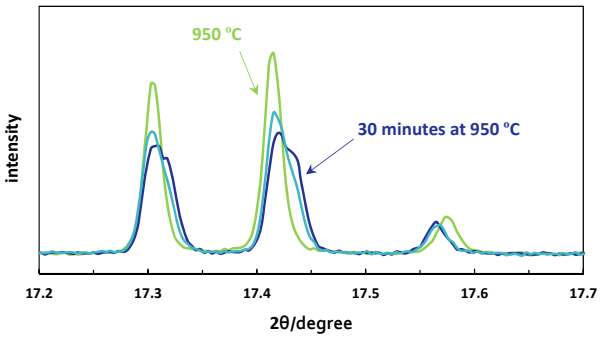

Fig. 9 Evolution of diffraction patterns of LAGP phase (rhombohedral) by holding the sample at 950 °C.

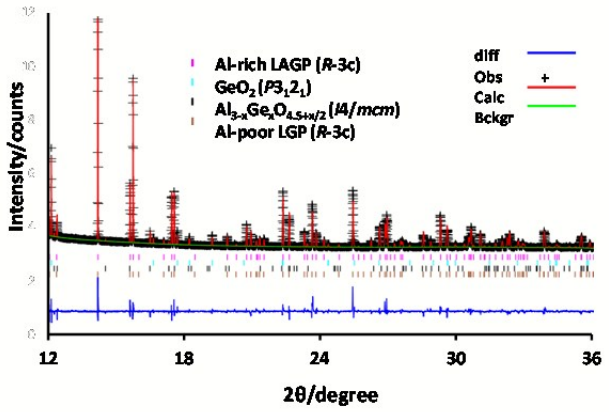

Fig. 10 Rietveld refined powder s-XRD pattern for the sample at 950 ^{0}C, (+++) observed, (—) calculated and difference. Vertical bars correspond to the calculated Bragg reflections from R-3c model for LAGP, $P3_12_1$ for GeO_2, I4/mcm for $Al_{3-x}Ge_xO_{4.5+x/2}$ and R-3c for LGP (from top to bottom).

could not find any sign of such a transition with the phase mixture at 950 °C – one containing Al-rich and Al-poor LAGP and the mullite, upon cooling. Instead the observed changes in the patterns may be understood as a change in the Al-distribution convoluted with thermal contraction.

Fig. 12 shows the changes in the lattice parameter *c* of the main NASICON phase during cooling to room temperature. As mentioned above, after the dwell time at 950°C both Al-rich and Al-poor rhombohedral phases are present in the structure. The lattice parameter and phase fraction variations imply that Al is redistributed during the cooling of the sample from the Al-rich phase (core) to the Al-poor phase (surface) making the particles again more homogenous. At the same time there is a reduction in the phase fraction of the mullite phase, so that some Al will also be redistributed to the LGP phase from there. Still, the Al content of the final NASICON-phase will be lower than the initial Al value of the core and this decrease contributes to the shrinkage along the *c* axis. Once the equilibrium is reached (in our samples we estimate around 300 °C), further changes in the lattice parameters are only caused by thermal expansion. During the cooling cycle, lithium pyrophosphate is again formed in the sample at around 750 °C, the same temperature as on heating. A phase transition around 630 ºC is observed for the peaks of this lithium salt, which agrees with the literature.[44] The formation of this phase may be attributed to the excess amount of lithium (extra 10 wt% in the form of Li_2CO_3) used during the synthesis process. Our *in situ* data now reveal that the Al-rich impurity phase germanium mullite $Al_{3-x}Ge_xO_{4.5+x/2}$, that is formed while keeping the sample at (too) high temperatures on cooling is reduced in phase fraction and the remaining mullite phase subsequently transforms to $AlPO_4$ ($P3_12_1$) at about 300 °C. Thokchom et al. have also experimentally reported (from ex situ room temperature XRD data) a partial decomposition of LAGP phase into $AlPO_4$ after having kept the sample at 950 °C for 6 hours.[2] According to the Rietveld analysis of the final room temperature s-XRD pattern, rhombohedral LAGP is the dominant crystalline phase along with GeO_2, $AlPO_4$ and $Li_2P_4O_7$ as impurity phases (Fig. 13).

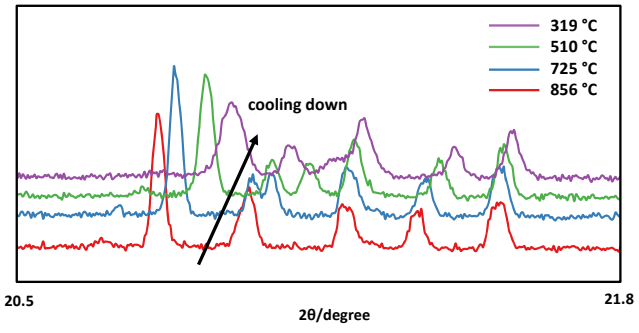

Fig. 11 Selected s-XRD patterns for the sample while cooling to highlight the phase transition.

Hence, by maintaining the annealing temperature sufficiently below 950 °C, the formation of germanium mullite and consequentially also of $AlPO_4$ could be eliminated. This observation also explains why differences in the heat treatment procedures translate into different deviations between the nominal and actual Al content (and hence different conductivity values) of the LAGP samples.

To further test the guidelines derived from the *in situ* synchrotron results, we synthesized *ex situ* samples and annealed them at different temperatures in the range of 650 °C to 900 °C and the effect of annealing temperature on the conductivity was investigated. In general we found the same trends, yet with a shift by about 50 °C in furnace temperatures, which may be due to the use of a different furnace as well as the faster heating (10 °C /min) and natural cooling rates

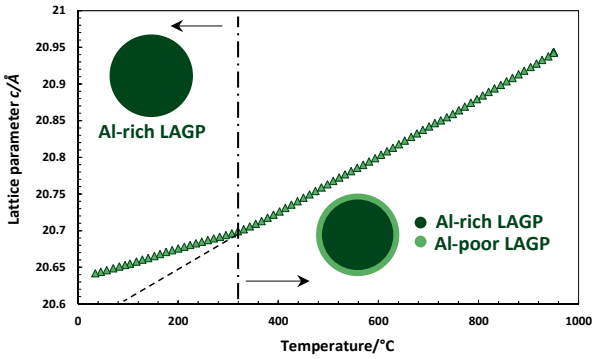

Fig. 12 Evolution of lattice parameter *c* during the cooling cycle.

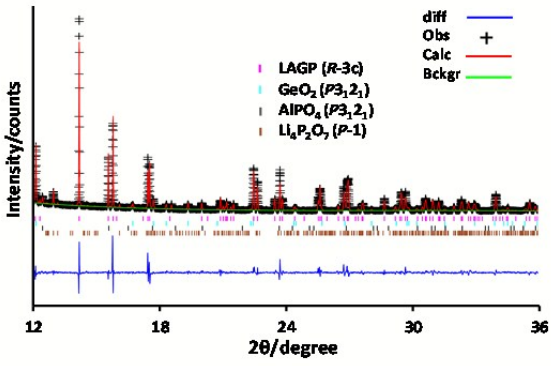

Fig. 13 Rietveld refined powder s-XRD pattern for the sample at room temperature (+++) observed, (—) calculated and difference. Vertical bars correspond to the calculated Bragg reflections from *R*-3*c* model for LAGP (top), $P3_12_1$ model for GeO_2 and $AlPO_4$ and *P*-1 for $Li_4P_2O_7$.

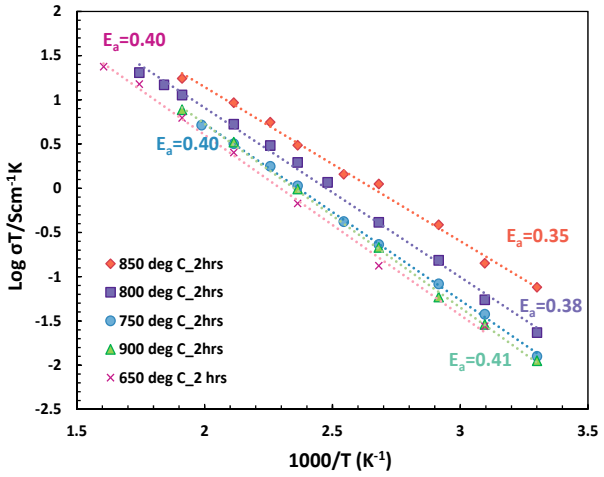

Fig. 14 Arrhenius plot of total conductivity for different annealing temperatures

employed. As seen in Fig. 14, the highest values of activation energy and lowest conductivities are found for the samples annealed at 650 °C (E_a = 0.40 eV) and 900 °C (E_a = 0.41 eV). As discussed above and shown in Fig. 5, increasing the annealing temperature promotes the formation of the fast-ion conducting LAGP phase in the pellets resulting in an enhancement of the conductivity and a slight reduction in the activation energy. For annealing temperatures below 800 °C *in situ* synchrotron data showed that the existence of an amorphous phase in the sample is one of the reasons behind higher activation energy. For the *ex situ* measurements the same applies to samples annealed below 750 °C. In addition the lower content of Al and its inhomogeneous distribution will contribute to the lower conductivity values found in the samples annealed at low temperatures.

The lowest activation energy (E_a=0.35 eV) and highest conductivity was achieved for the *ex situ* sample annealed at 850 °C. The observed decrease in conductivity when the annealing temperature exceeds this value (here to 900 °C), can now be understood as a consequence of the extraction of Al from LAGP phase and formation of impurity phase of $AlPO_4$. Fig. 15 compares the lattice parameters *a* and *c* for different annealing temperatures. As shown here, by increasing the annealing temperature, lattice parameter *a* decreases (especially between 700 °C and 750 °C where the amorphous phase vanishes) and lattice parameter *c* increases. Factoring in the slight shift in optimum annealing temperatures between the two heat treatment series discussed above, the overall trends of the *ex situ* diffraction and conductivity experiments are in good agreement with *in situ* diffraction data. An increase in Al incorporation into the LAGP phase with increasing annealing temperature yields larger room temperature values of the lattice parameter *c* (cf. Fig. 7) and enhanced conductivities. Similarly, the drop in lattice parameter *c* when the annealing temperature is increased to 900 °C can be attributed to the extraction of Al from LAGP (c.f. Fig. 8) and linked to a drop in conductivity.

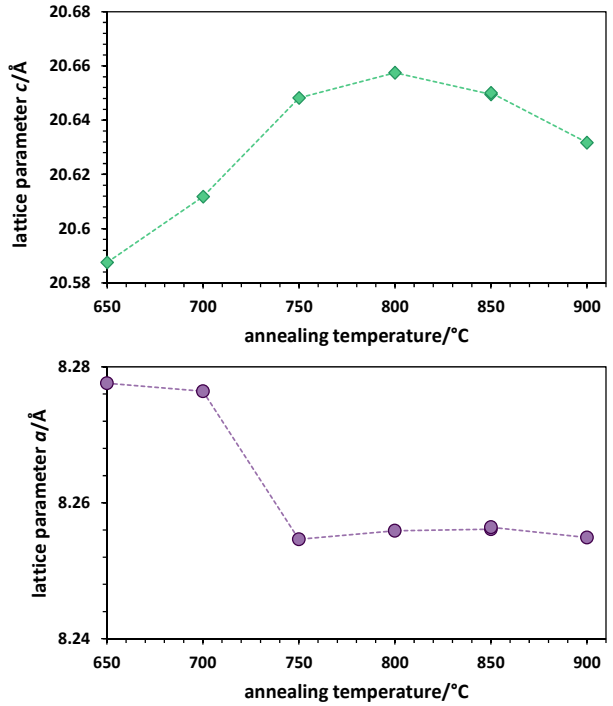

Fig. 15 Variation in the lattice parameters *a* and *c* with annealing temperature

To demonstrate the favourable performance of the LAGP produced according to the synthesis guidelines elaborated in this work, we employed a 2 mm thick LAGP pellet as anode-protecting membrane in a hybrid Li-air cell. Here "hybrid" refers to the use of an aqueous catholyte (here 5M LiOH) and an organic anolyte (1M $LiPF_6$ in EC/DMC) separated by the ceramic Li^+ ion conductor LAGP. Oxygen reduction/evolution at the air cathode is catalyzed through finely dispersed Pt on multi-walled carbon nanotube arrays. Cycling performance of the cell is shown in Fig. 16. When each cycle is limited to 40 minutes with a current of 0.03 mAcm^{-2} the hybrid cell retains its charge and discharge capacity for 140 cycles with <0.1V polarization between charge/discharge for the first 70 cycles and hence an energy efficiency > 97%.

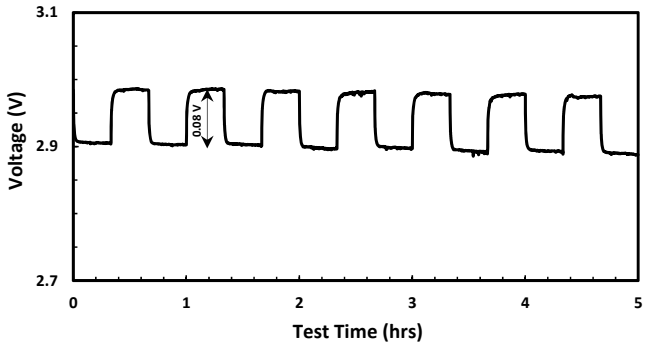

Fig. 16 Room temperature cycling performance of hybrid Li-air cell with LAGP ceramic as anode-protecting membrane at constant current of 0.03 mAcm^{-2} (each cycle is limited to 40 minutes)

Conclusions

A detailed *in situ* synchrotron XRD study is conducted to rationalize and improve the synthesis process of NASICON-type $Li_{1+x}Al_xGe_{2-x}(PO_4)_3$ ceramics and to produce phase pure LAGP with effective Al doping that should yield maximum ionic conductivity. Results are closely correlated to and provide straightforward explanations for the variation in the properties of *ex situ* samples with the respective annealing conditions. Sequential Rietveld refinements of the *in situ* data reveal that even though the sample starts to crystallise at around 570 °C, effective Al incorporation into the LAGP structure requires prolonged heating to about 800 °C. At the early stages of crystallisation, Al-poor LGP is the dominant phase but gradually vanishes with further heating of the sample resulting in a more homogenous structure. On the other hand, heating the sample to high temperatures (≈950 °C), results in the extraction of Al from the outer shell of LAGP particles and the formation of an impurity phase, germanium mullite. Germanium mullite, upon cooling, decomposes into $AlPO_4$ and is in part responsible for significant deviations of the Al-content in LAGP and final product compositions. The result of this study along with the literature data permitted us to establish a correlation between lattice parameter '*c*' and the amount of Al content in LAGP generally and this can be used to estimate the actual concentration of Al dopant in the structure at room temperature.

Acknowledgements

This research was supported by the National Research Foundation, Prime Minister's Office, Singapore under its Competitive Research Programme (CRP Awards NRF-CRP 10-2012-6 and NRF-CRP 8-2011-4). NS would like to thank AINSE Ltd for providing support through the research fellowship scheme and the Australian Research Council (DE160100237). Part of this research was undertaken on the Powder Diffraction beamline at the Australian Synchrotron, Victoria, Australia.

References

1. E. Quartarone and P. Mustarelli, *Chem. Soc. Rev*, 2011, **40**, 2525-2540.
2. J. S. Thokchom, N. Gupta and B. Kumar, *J. Electrochem. Soc.*, 2008, **155**, A915-A920.
3. M. Balaish, A. Kraytsberg and Y. Ein-Eli, *PCCP*, 2014, **16**, 2801-2822.
4. A. Manthiram and L. Li, *Adv. Energy Mater.*, 2015, **5**, 1401302.
5. S. Adams and R. P. Rao, *J. Mater. Chem.*, 2012, **22**, 1426-1434.
6. R. P. Rao, W. Gu, N. Sharma, V. K. Peterson, M. Avdeev and S. Adams, *Chem. Mater.*, 2015, **27**, 2903-2910.
7. V. Thangadurai, H. Kaack and W. J. F. Weppner, *J. Eur. Ceram. Soc.*, 2003, **86**, 437-440.
8. R. P. Rao and S. Adams, *Phys. Status Solidi A*, 2011, **208**, 1804-1807.
9. R. P. Rao, N. Sharma, V. K. Peterson and S. Adams, *Solid State Ionics*, 2013, **230**, 72-76.
10. S. Adams and R. Prasada Rao, *J. Mater. Chem.*, 2012, **22**, 7687-7691.
11. M. Chen, X. Yin, M. V. Reddy and S. Adams, *J. Mater. Chem. A*, 2015, **3**, 10698-10702.
12. M. Chen and S. Adams, *J Solid State Electrochem*, 2015, **19**, 697-702.
13. P. Knauth, *Solid State Ionics*, 2009, **180**, 911-916.
14. N. Imanishi and O. Yamamoto, *Materials Today*, 2014, **17**, 24-30.
15. M. Zhang, K. Takahashi, N. Imanishi, Y. Takeda, O. Yamamoto, B. Chi, J. Pu and J. Li, *Journal of The Electrochemical Society*, 2012, **159**, A1114-A1119.
16. L. Truong and V. Thangadurai, *Chem. Mater.*, 2011, **23**, 3970-3977.
17. C. Liu, K. Rui, C. Shen, M. E. Badding, G. Zhang and Z. Wen, *J. Power Sources*, 2015, **282**, 286-293.
18. A. Boulant, J. F. Bardeau, A. Jouanneaux, J. Emery, J.-Y. Buzare and O. Bohnke, *Dalton Transactions*, 2010, **39**, 3968-3975.
19. B. Lang, B. Ziebarth and C. Elsässer, *Chem. Mater.*, 2015, **27**, 5040-5048.
20. K. Arbi, R. Jimenez, T. Šalkus, A. Orliukas and J. Sanz, *Solid State Ionics*, 2015, **271**, 28.
21. K. Arbi, M. Hoelzel, A. Kuhn, F. Garcia-Alvarado and J. Sanz, *Inorg. Chem.*, 2013, **52**, 9290.
22. D. Rettenwander, A. Welzl, S. Pristat, F. Tietz, S. Taibl, G. J. Redhammer and J. Fleig, *J of Mater. Chem. A*, 2016, DOI: 10.1039/C5TA08545D.
23. Y. Shimonishi, T. Zhang, N. Imanishi, D. Im, D. J. Lee, A. Hirano, Y. Takeda, O. Yamamoto and N. Sammes, *J. Power Sources*, 2011, **196**, 5128-5132.
24. Y. Liu, B. Li, H. Kitaura, X. Zhang, M. Han, P. He and H. Zhou, *ACS Appl Mater Interfaces*, 2015, DOI: 10.1021/acsami.5b04409.
25. T. Zhang, N. Imanishi, Y. Shimonishi, A. Hirano, Y. Takeda, O. Yamamoto and N. Sammes, *Chem. Commun.*, 2010, **46**, 1661-1663.
26. A. Aboulaich, R. Bouchet, G. Delaizir, V. Seznec, L. Tortet, M. Morcrette, P. Rozier, J.-M. Tarascon, V. Viallet and M. Dollé, *Adv. Energy Mater.*, 2011, **1**, 179-183.
27. Y. Kobayashi, S. Seki, M. Tabuchi, H. Miyashiro, Y. Mita and T. Iwahori, *J. Electrochem. Soc.*, 2005, **152**, A1985-A1988.
28. K. Arbi, J. M. Rojo and J. Sanz, *J. Eur. Ceram. Soc.*, 2007, **27**, 4215.
29. A. Aatiq, M. Menetrier, L. Croguennec, E. Suard and C. Delmas, *J. Mater. Chem.*, 2002, **12**, 2971-2978.
30. M. Alami, R. Brochu, J. L. Soubeyroux, P. Gravereau, G. Le Flem and P. Hagenmuller, *Journal of Solid State Chemistry*, 1991, **90**, 185-193.
31. L.L. Wong, H.M. Chen and S. Adams, *in preparation*.
32. J. Fu, *Solid State Ionics*, 1997, **104**, 191-194.
33. J. Fu, *Solid State Ionics*, 1997, **96**, 195-200.
34. C. Schröder, J. Ren, A. C. M. Rodrigues and H. Eckert, *The Journal of Physical Chemistry C*, 2014, **118**, 9400-9411.
35. K. Arbi, W. Bucheli, R. Jiménez and J. Sanz, *J. Eur. Ceram. Soc.*, 2015, **35**, 1477-1484.
36. D. Safanama, D. Damiano, R. P. Rao and S. Adams, *Solid State Ionics*, 2014, **262**, 211-215.

37. K. S. Wallwork, B. J. Kennedy and D. Wang, *API Conference Proceeding*, 2007, 879-882.
38. D. Richard, M. Ferrand and G. J. Kearley, *Journal of Neutron Research*, 1996, **4**, 33-39.
39. A. C. Larson and R. B. Von Dreele, *Los Alamos National Laboratory Report (LAUR)*, 2004, 86-748.
40. B. H. Toby, *J. Appl. Cryst.*, 2001, **34**, 210-213.
41. C. R. Mariappan, C. Yada, F. Rosciano and B. Roling, *J. Power Sources*, 2011, **196**, 6456-6464.
42. Z. Liu, S. Venkatachalam and L. van Wüllen, *Solid State Ionics*, 2015, **276**, 47-55.
43. E. R. Losilla, M. A. G. Aranda, M. Martínez-Lara and S. Bruque, *Chem. Mater.*, 1997, **9**, 1678-1685.
44. M.-T. Averbuch-Pouchot and A. Durif, *Topics in Phosphate Chemistry*, World Scientific Publishing Co. Pte. Ltd. .

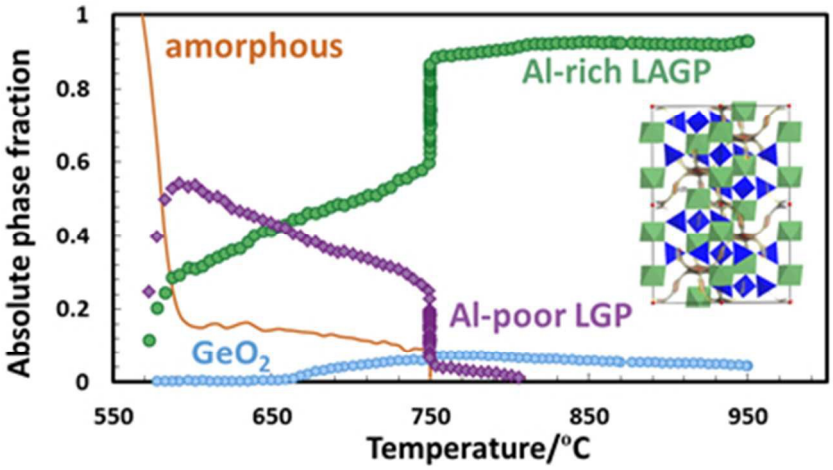

72x40mm (150 x 150 DPI)